RSC Advances

PAPER

View Article Online
View Journal | View Issue

Cite this: *RSC Adv.*, 2026, **16**, 2271

Millable polyurethane/cellulose acetate/nanohydroxyapatite composite film as a flexible ferro-piezoelectric nanogenerator for innovative applications in physiological motion sensing

Gopika Melepalliyalil,[a] Mekha Mariam Mathew,[a] Soney Varghese[b] and Unnikrishnan Gopalakrishna Panicker *[a]

The advancement of piezoelectric nanogenerators capable of converting mechanical energy into electrical energy holds the potential for remarkable progress in biomedical devices and wearable consumer electronics. The current research work delves into the development of innovative polymeric piezoelectric composites intended for applications in energy harvesting and physiological motion sensing. The study explores the feasibility of a system composed of a millable polyurethane (MPU)/cellulose acetate (CA) blend reinforced with nanohydroxyapatite (nHA) to create a flexible ferro-piezoelectric polymer composite material. MPU and CA have been blended to create a polymer blend matrix, which has subsequently been embedded with nHA quantitatively. Morphology, mechanical strength, chemical features, and crystalline characteristics have also been systematically analyzed. The composite films exhibit piezoelectric properties, as evidenced by butterfly-shaped amplitude curves obtained from dynamic contact electrostatic force microscopy. Polarization measurements corresponding to the applied electric field validate the presence of ferroelectric domains in the resulting P–E hysteresis curves. An assessment of dielectric property variation has also been conducted as a function of frequency. A device prototype is manufactured, and tribo-piezoelectric responses, along with the resulting voltage generated in response to human finger tapping, have been evaluated using a digital oscilloscope. The outcomes offer valuable insights into the promising potential of creating efficient piezoelectric nanogenerators from this novel system, applicable across a spectrum of commercial utility.

Received 7th November 2025
Accepted 29th December 2025

DOI: 10.1039/d5ra08584e

rsc.li/rsc-advances

1. Introduction

The exacerbating effects of population growth and over-consumption of non-renewable energy sources like fossil fuels are now raising mounting concerns related to the availability of adequate energy for future generations.[1] A potential solution to get around these challenges might be utilizing energy from renewable sources. Mechanical energy harvesting presents a promising avenue for enabling wearable electronics and low-power sensor networks. The growing preference for durable, low-power portable smart devices has fueled interest in harnessing energy from inexpensive sources like body motion and material friction.[2–5] A piezoelectric nanogenerator (PENG) captures mechanical energy from small-scale vibrations, movements, or pressure changes and converts it into electrical energy.[6,7] Developing piezoelectric energy harvesting (PEH) devices for small electronic devices, powered by human body movements such as walking, running, breathing, tapping, and dancing, represents an interesting research domain focused effort in this direction.[4,7,8]

Common piezoelectric ceramics, such as lead zirconate titanate (PZT), and lead titanate, find applications across various fields. Despite their remarkable efficiency in converting mechanical energy into electrical energy due to high piezoelectric coefficients, their toxic lead content poses risks to both human health and the environment.[9] Although lead-free piezoceramics exist, they come with notable downsides such as high density, brittleness, rigidity, and limited flexibility; restricting their usage in energy-related applications that demand flexibility. Polymers are a favorable choice for numerous applications requiring flexibility, owing to their mechanical viability, ease of processing, and cost-effectiveness[10–12] Among the prominent piezoelectric polymers, polyvinylidene fluoride (PVDF) and its derivatives, typically

[a]*Polymer Science and Technology Research Laboratory, Department of Chemistry, National Institute of Technology Calicut, Calicut, Kerala 673601, India. E-mail: unnig@nitc.ac.in*

[b]*Nanomaterials and Devices Research Laboratory, Department of Materials Science and Engineering, National Institute of Technology Calicut, Calicut, Kerala 673601, India*

polyvinylidene fluoride–trifluoroethylene (PVDF–TrFE), have garnered significant attention; emerging as competitive substitutes for current ceramic systems.[12,13] However, in polymers like PVDF, the requirement for the crucial β-phase responsible for the piezoelectric effect necessitates alignment with polar domains through a poling process. This step, while effective, may not be universally suitable; due to the complexities in processing and other potential obstacles such as low piezoelectric coefficients and mechanical strength.[13,14] In recent years, researchers have devised strategies to enhance piezoelectric materials by employing polymer composites and nanocomposites. This involves dispersing metal oxide, carbon-based, and ceramic fillers within a polymer matrix.[15,16] In comparison to solely ceramics and pure polymer materials, the composites exhibit several improved properties. With their adaptability, low weight, and ability to harvest energy from diverse sources, piezoelectric nanogenerators based on polymer nanocomposites prove ideal for a broad range of application, including wearable products and self-powered sensors.[17–19]

Chung *et al.*[20] employed screen printing and reactive zinc hydroxo-condensation to produce a flexible thin film piezoelectric nanogenerator through a solution-processing method. They crafted a highly elastic thin film, allowing the piezoelectric unit to generate energy through mechanical rolling and stretching. Pi and colleagues[21] developed a flexible nanogenerator using a spin-coated thin film of poly(vinylidene fluoride-*co*-tetrafluoroethylene) (PVDF–TrFE) as a functional layer on a polyimide substrate. Their investigation meticulously characterized the cyclic stretching-releasing process and assessed the impact of strain rate on the nanogenerator's electrical outputs. Sanches *et al.*,[22] employing solution casting and compression, created flexible piezoelectric three-phase nanocomposites. The composites included cellulose nanocrystals as the third phase, lead zirconate titanate as a second phase, and water-based polyurethane as the matrix. Cellulose nanocrystals served as a reinforcement to enhance dispersant strength, local conductivity control, and the polarization effect of ceramic grains within the matrix. Friere *et al.*[23] evaluated the influence of multiwalled carbon nanotubes (MWCNTs) on the electrical, dielectric, and piezoelectric properties of ferroelectric ceramic/castor-oil polyurethane (PUR) composite films. Yan and colleagues[24] recently developed high-performance triboelectric nanogenerators (TENGs) for diverse applications. Their study suggests the possible fabrication of flexible high-performance TENGs, containing an ethyl cellulose/thermoplastic polyurethane (EC/TPU) nanofiber triboelectric layer with barium titanate (BTO) nanoparticles as fillers.[24] Li *et al.* fabricated a flexible nanogenerator using electrospun PVDF/cellulose acetate (CA) composite membranes. They adjusted the CA-PVDF ratios to enhance the β-phase content and piezoelectric response.[25] Several natural materials capable of converting mechanical energy into electrical output have gained significant attention because they offer low-cost processing, ecological safety, and biocompatibility during continuous or intermittent contact with the human body. Hydroxyapatite (Ca_{10} $(PO4)_6$ $(OH)_2$) is one of the most important bio-ceramics used in bone and dental applications due to its excellent biocompatibility, bioactivity, and chemical similarity to the mineral component of human bone.[26] It exhibits high surface polarity, abundant functional groups, and tunable surface charge, which enable strong interfacial interactions within polymer matrices.[27] Sathiyanathan *et al.* successfully crafted a piezoelectric sensor (PSB) to monitor human respiratory behavior.[28] They explored piezo-responsive behaviors of electrospun polyvinylidene fluoride (PVDF) systems, including PVDF/polyoctafluoropentyl acrylate (PVDF–PFA), and PVDF-PFA/hydroxyapatite (HAP) systems, considering a nanoweb stacking arrangement. They investigated the impact of varying HAP content on the molecular orientation of CH_2–CF_2 dipoles in PVDF-PFA/HAP blends. Our group utilized the electrospinning technique to create piezoelectric polymer mats from ethylene-*co*-vinyl acetate–millable polyurethane/nanohydroxyapatite (EVA–MPU/nHA) composite systems.[29] Electrostatic force microscopy confirmed the ferro-piezoelectric characteristics of the samples, indicating a promising route for developing user-friendly piezoelectric mats for physiological motion-sensing applications.

Though many interesting articles are available in the literature, there is currently no report on the piezoelectric capabilities of solution-casted MPU/CA/nHA composites. This study fills that void by presenting the development of cost-effective tribo-piezoelectric/ferroelectric nanogenerators capable of harnessing energy from human physical movements. A strategic combination of two commercially significant polymers, *viz*; millable polyurethane (MPU) and cellulose acetate (CA), both exhibiting substantial dielectric constants, has been chosen for the matrix development. Polyurethanes (PUs) are well known for their biocompatibility, mechanical flexibility, and highly tunable chemical structure. Their elastic and skin-friendly properties facilitate comfortable use in wearable sensors and motion-monitoring devices.[30] Cellulose acetate (CA), a derivative of natural cellulose, is known for its excellent biocompatibility, non-toxicity, and environmental safety. Its semi-synthetic structure provides a balance of mechanical flexibility, breathability, and chemical stability, making it suitable for prolonged contact with the human body. CA is also partially biodegradable, offering a safer and more sustainable option for biocompatible energy-harvesting systems.[31] Nano-hydroxyapatite (nHA) has been introduced to functionally modify the matrix. MPU, with its adaptable physicochemical properties, possesses high strain tolerance and hence is ideal for applications requiring multiple bending or twisting.[32,33] Meanwhile, CA can contribute to the composite's mechanical stability, biocompatibility, and film-forming tendencies.[30] As a dielectric and lead-free piezoelectric material, nHA has gained prominence in recent years; capable of generating dipolar polarization or orientation due to its positively charged 'a' plane and negatively charged 'c' plane.[34–37] Additionally, the cellulose acetate component provides inherent tribonegative sites, the elastic MPU matrix facilitates deformation-induced charge separation, and the incorporated nHAp nanoparticles introduce polar surfaces and micro-roughness that increase local charge density.[38,39] The overall objective of this work is to create a flexible piezoelectric polymer nanocomposite being tailored for the development of piezoelectric nanogenerators (PENGs) for energy harvesting and

physiological motion sensing applications. The characterization has been done with FTIR, SEM, XRD, UTM, TGA, and impedance analysis. Ferroelectric and piezoelectric performances are assessed through DC-EFM and ferroelectric testing.

2. Experimental section

2.1. Materials

Millable polyurethane (Premilled Millathane E34) with polyether soft segments and toluene diisocyanate hard segments with a Mooney viscosity of 45 ± ML at 100 °C, was procured from Vajra Rubber Products, Thrissur, India, while cellulose acetate (average M.W. 100 000 g mol^{-1}) was obtained from Thermo Fisher Scientific, India. A wet chemical method was followed in our laboratory to synthesize nanohydroxyapatite particles.[40] The calcium nitrate tetrahydrate ($Ca(NO_3)_2 \cdot 4H_2O$, ≥ 99% purity) and dibasic ammonium phosphate ($(NH_4)_2HPO_4$, 99.5% purity) salts were utilized as calcium and phosphorus sources; obtained from Merck, India. Ammonium hydroxide solution (25% NH_3) was acquired from Qualigens, India. Chloroform (≥99%), used as a solvent for polymer solution preparation in the casting process, was sourced from Merck, India. Additionally, conductive copper foil and metallic wires for piezoelectric device fabrication were obtained from Icoolbear, India.

2.2. Preparation of nanohydroxyapatite

The nanohydroxyapatite (nHA) was synthesized in the laboratory through a wet chemical method using $Ca(NO_3)_2 \cdot 4H_2O$ and $(NH_4)_2HPO_4$ as precursors.[40,41] The precursor solutions were prepared separately; maintaining a theoretical apatitic ratio of calcium to phosphorous (Ca/P) at 1.67. The Ca^{2+} solution was adjusted to a pH of 11 by adding ammonia solution. The phosphate solution was then slowly added dropwise, with continuous magnetic stirring at 80 °C and ultrasonication. The mixture was left to age for 24 hours, and the formed precipitate was washed with distilled water until all traces of ammonia were

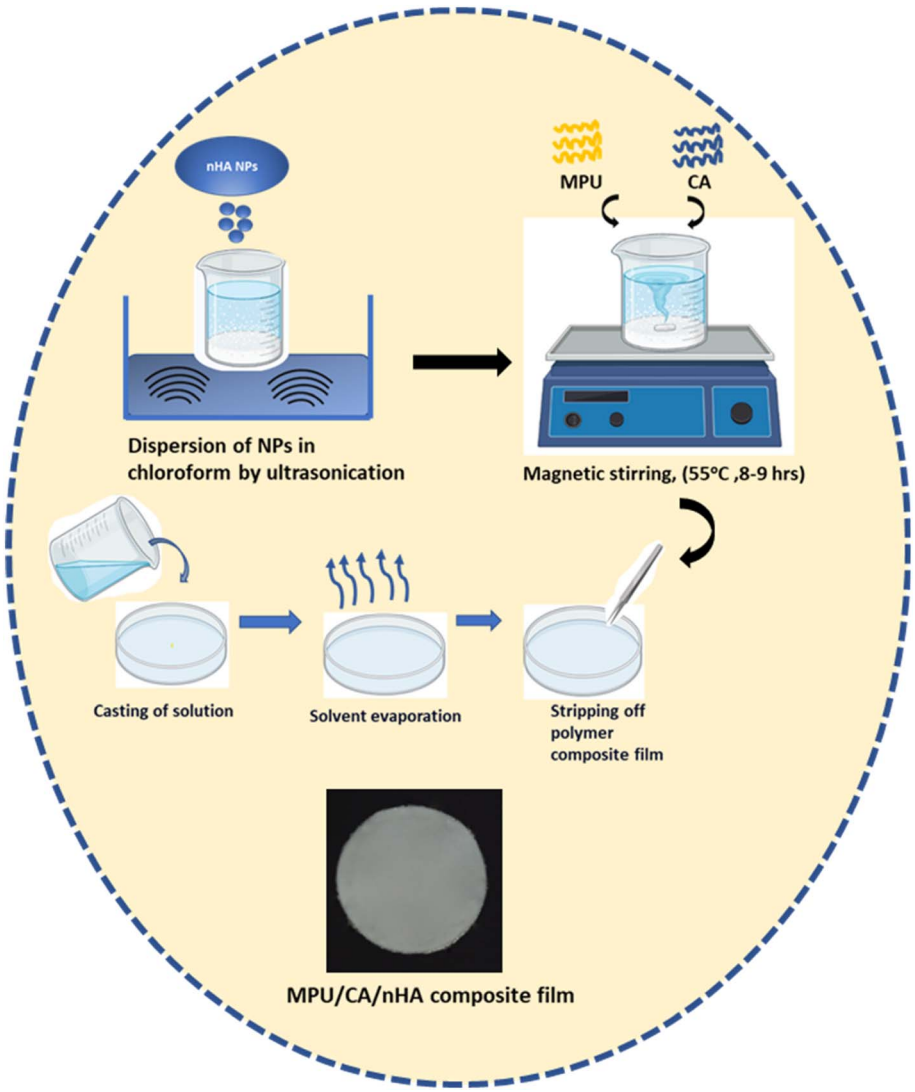

Fig. 1 Schematic representation for the preparation of MPU/CA/nHA composite films.

Table 1 Sample formulations

Sl NO.	MPU (%)	CA (%)	nHA (phr)	Sample code
1	80	20	0	82 MC
2	80	20	2	MCH2
3	80	20	4	MCH4
4	80	20	6	MCH6
5	80	20	8	MCH8
6	80	20	10	MCH10

removed. The collected precipitate was dried at 80 °C, and then calcination at 550 °C for 3 hours. Subsequently, ball milling was carried out to achieve fine hydroxyapatite nanoparticles.

2.3. Preparation of MPU/CA/nHA composite films

To create the nanocomposite films, nanohydroxyapatite (nHA) particles were initially dispersed in chloroform using an ultrasound bath, followed by magnetic stirring. Millable polyurethane (MPU) and cellulose acetate (CA) were then dissolved in the solvent containing the dispersed nanoparticles and subjected to magnetic stirring at a temperature of 55 °C for 8 hours until a uniform solution was achieved. This solution was poured onto a suitable glass Petri dish (100 mm in diameter), and the films were dried in a hot air oven within a temperature range of 60–70 °C. After cooling, the nanocomposite films were peeled off from the glass Petri dish. Similar successful solvent casting protocols have been reported by our group earlier.[42,43] A schematic representation of the nanocomposite film preparation is presented in Fig. 1, and the compositions developed are detailed in Table 1.

2.4. Characterization

An infrared (IR) spectrometer (JASCO FTIR 4700) was used to record the spectra of nHA particles and composite films in the attenuated total reflection (ATR) mode. Scans were performed in the range of 4000–400 cm^{-1} for each sample. X-ray diffraction analysis was performed to study the crystalline features and phase purity of the synthesized nHA particles and nHA-loaded composite films; by using an X-ray diffractometer (Rigaku Miniflex 600) Cu K radiation with a wavelength of 1.54 Å at a scan rate of 5° min^{-1} and an operating voltage of 40 kV. Field-emission scanning electron microscopy (FESEM, Gemini SEM 300, Carl Zeiss) was used to analyze the morphology of the composite films. The size and morphology of the prepared nHA particles were analyzed using FE-SEM and elemental composition; with an EDS (Gemini 300/EDS). The mechanical features of the composite films were examined using a Universal Testing Machine (UTM, Shimadzu Auto graph, AG-Xplus series, Japan) with a 10 N stress. ASTM 412 was followed to prepare the samples. The thermal stability was analyzed by using a thermogravimetric analyzer (Q50-TA Instruments, USA) between 25 to 650 °C at a heating rate of 10 °C min^{-1}. Atomic force microscopy (AFM) was used in dynamic-contact electrostatic force microscopic mode (DC-EFM) to investigate the piezoelectric and ferroelectric properties of the composites (Park XE100, Park systems) with a voltage sweep from −10 to 10 V. For the tapping mode, a cantilever (NSC14-Cr/Au) with a radius of curvature less than 50 nm, a resonant frequency of 160 Hz, and a spring constant of 1.8 N/m was used. The dielectric properties of the samples were analyzed by using an impedance analyzer (4192 A, Agilent Technologies, Palo Alto, CA) at a frequency range of 40–10^6 Hz; with samples of average 0.5 mm thickness. Ferroelectric features were analyzed from P–E hysteresis curves obtained by measuring the resultant polarisation by the application of an electric field from −200 V to 200 V (Precision RT66C ferroelectric tester, RT66C0819-143 (200 V)).

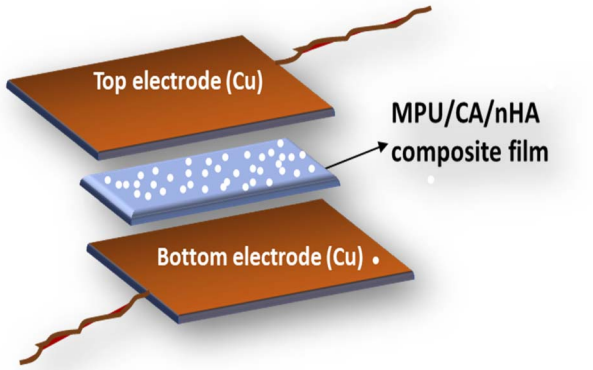

Fig. 2 Fabrication of device for output voltage testing.

2.5. Device fabrication and output voltage testing

A device prototype was fabricated by sandwiching the composite films (1 cm × 1 cm area and 0.5 mm thickness) between conductive copper foils attached to metallic wires. A digital storage oscilloscope (Tektronix, TBS 2000series) was employed to assess the voltage output corresponding to the mechanical force applied through random human finger tapping (1.5–2 N) of the fabricated PENGs. The device fabrication is illustrated in Fig. 2.

3. Results and discussion

3.1. FTIR and XRD analysis of nanohydroxyapatite

FTIR spectra of the synthesized nanohydroxyapatite, recorded at 400–4000 cm^{-1}, are shown in Fig. 3a. The distinctive stretching peak of hydroxyl (OH^-) is visible at 3570 cm^{-1}, indicating that the synthesized hydroxyapatite was in the pure phase.[44] At 1060 cm^{-1}, the stretching vibration (P–O–P) peaks of phosphate (PO_4^{3-}) are observed. P–O bending vibrations are seen at 632 and 561 cm^{-1}. The OH stretching for physically absorbed water is represented by the peaks at 1636 and 3232 cm^{-1}.[45] The findings are in full compliance with the previously published articles.[35,37] The XRD data for nHA was recorded at 2θ from 10 to 60°. In the XRD patterns shown in Fig. 3b, the (002), (210), (211), (112), (300), (202), (222), (213) and (004) planes of nHA samples are observed at 2θ angles of 25.8,

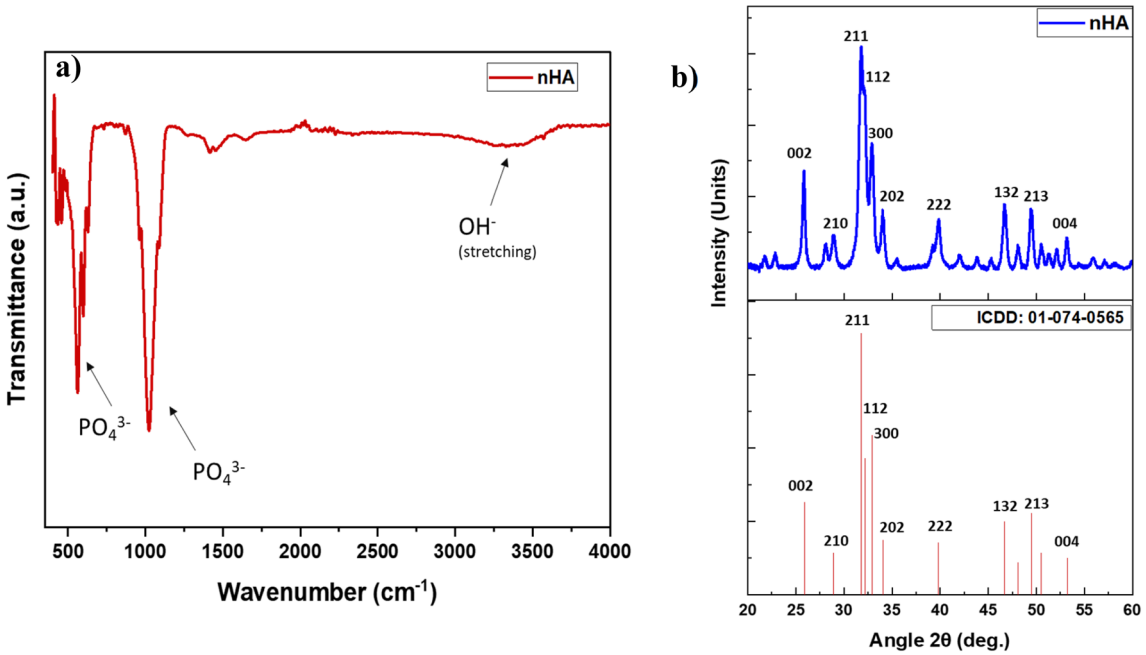

Fig. 3 (a) FTIR spectra of nHA (b) XRD diffractogram of synthesized nHA particles with ICCD-01-074-0565.

28.9, 31.87, 32.9, 34.01, 39.87, 46.69, 49.58, and 53.18°, respectively; matching well with the ICCD-01-074–0565 file.[46]

The Scherer formula (eqn (1)) has been utilized to determine the average crystallite sizes:

$$D = \frac{k\lambda}{\beta\cos\theta} \quad (1)$$

where λ represents the X-ray radiation wavelength, θ denotes the peak's Bragg angle, and β represents the full width at half maximum (FWHM).[47] A theoretical value of 22 nm has been observed by considering the average crystallite sizes obtained from each of the distinct characteristic hydroxyapatite peaks.

3.2. SEM and EDS analysis of nHA

The theoretically calculated crystallite size of nano-hydroxyapatite (nHA) has been juxtaposed with the experimental value using SEM images illustrated in Fig. 4a. The nHA powder exhibits the typical morphology seen in powders of pure apatitic tricalcium phosphate [Ca10(PO4)6(OH)2]; comprising both individual nanoparticles and their agglomerates. The experimental crystallite size is determined as 24 nm, aligning closely with the theoretical value. Elemental analysis conducted through EDS mapping (Fig. 4b and c) further validates the presence of calcium and phosphate ions in a ratio of 1.6, which is the characteristic stoichiometric ratio of hydroxyapatite.[45]

3.3. FTIR and XRD analysis of MPU/CA/nHA composite films

The ATR-IR spectra of nanohydroxyapatite (nHA), the blend (82 MC), and the composite with 8 phr of nHA (MCH8) are depicted in Fig. 5a. Peaks observed at 630 cm^{-1} and 561 cm^{-1} correspond to P–O bending vibrations, while those at 961 and 1044 cm^{-1} correspond to P–O–P stretching vibrations. These observations confirm the presence of the $(PO4)^{3-}$ group in the nHA-filled composites.[43–46] A slight shift in the peaks is noted, attributed to polar-polar interactions between the filler and polymer matrix. Notably, these corresponding peaks are absent in the neat spectrum of the blend, confirming the modification of the blend with the inclusion of nHA filler particles.

Diffractograms of blend/nHA-filled composites are presented in Fig. 5b. A notable MPU peak at $2\theta = 20.2°$ is consistently observed in all samples, diminishing in intensity with the incorporation of nHA. This phenomenon suggests the potential intercalation of nHA within the polymer matrix, possibly leading to disruptions in the crystalline phases of the polymer matrix. The distinct peaks of nHA are identified at 25.8, 31.97, 33.13, 46.7, and 53°, corresponding to (002), (112), (300), (222), and (004) planes, respectively.[46] The observed shifting of peaks from their exact values is indicative of strong polar-polar interactions between the filler and matrix.

3.4. Morphology

Fig. 6 presents surface morphology of the composite films illustrating the dispersion of filler particles within the polymer matrix. Composite films containing up to 8 phr of nHA exhibit a smooth surface with a uniform morphology. However, at higher loadings, larger particles become visible, which could be attributed to the possible filler agglomeration at concentrations surpassing a threshold value within the matrix. The cross-sectional SEM images and EDAX mapping of the MCH8 composite (Fig. 6b and c) reveal a well-integrated and uniformly dispersed filler-matrix system. The low-magnification image shows a continuous and defect-free cross-section. At higher magnification, the images highlight that the nHA particles are homogeneously embedded within the polymer matrix

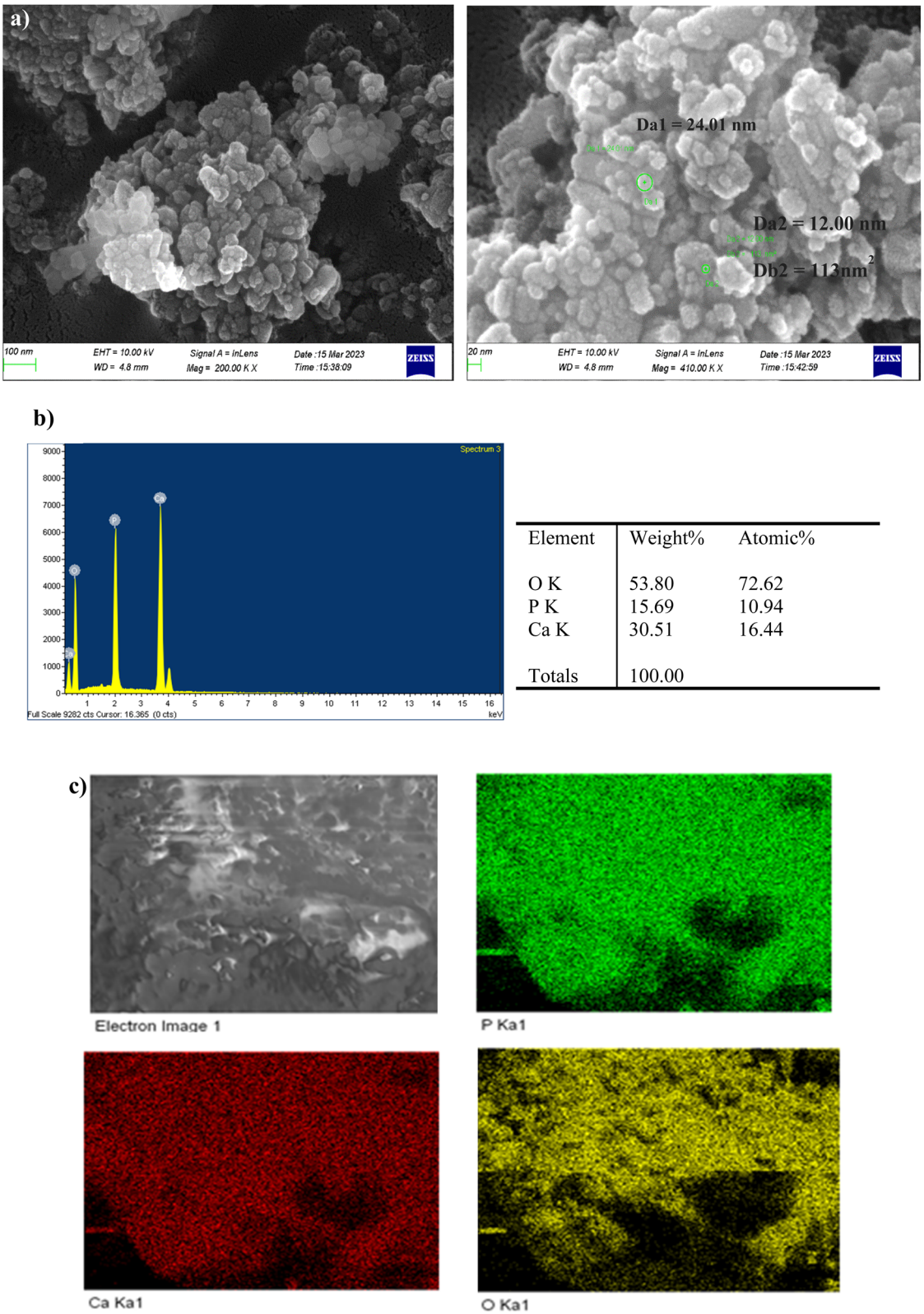

Element	Weight%	Atomic%
O K	53.80	72.62
P K	15.69	10.94
Ca K	30.51	16.44
Totals	100.00	

Fig. 4 (a) SEM micrographs of nHA (b) EDS analysis of nHA (c) EDS elemental mapping location from SEM.

without significant agglomeration. The roughened micro-texture and uniform particle distribution indicate effective wetting of nHA by the polymer blend, promoting multiple polymer-filler interfaces. These interfaces are critical for enhancing Maxwell–Wagner interfacial polarization and improving stress transfer during mechanical deformation.

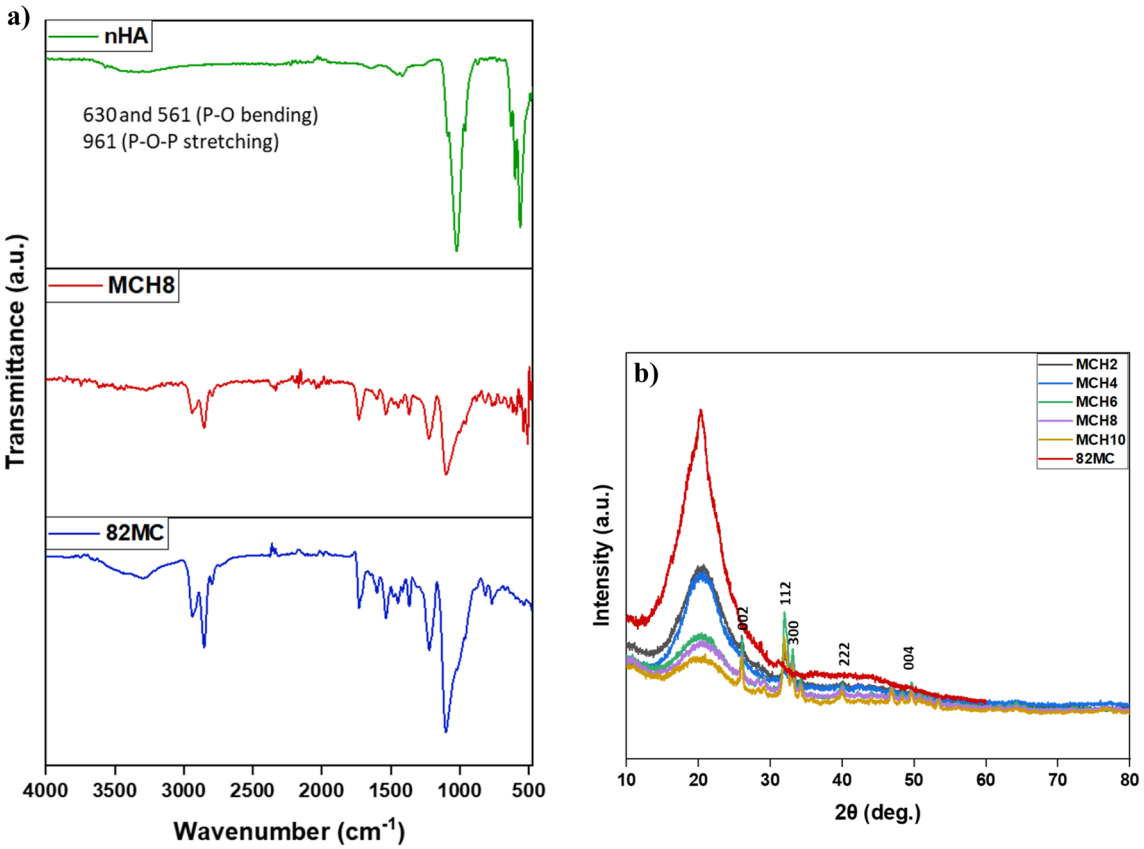

Fig. 5 (a) FTIR spectra of nHA powder, MPU/CA blend, and MPU/CA/nHA composite (b) XRD diffractograms of blend and nHA-loaded composite films.

3.5. Mechanical properties

The mechanical characteristics of the composite systems are illustrated Fig. 7a–d. The addition of nanohydroxyapatite (nHA) results in an improvement in both tensile strength and Young's modulus across all samples. Materials exhibiting enhanced mechanical properties, including strength and flexibility, are desirable for the fabrication of piezoelectric nanogenerators (PENGs). At lower to moderate filler loadings, well-dispersed nHA particles could serve as effective reinforcing agents. Therefore, achieving proper dispersion and alignment of fillers within a polymer matrix can enhance stress transfer within a film, leading to improved matrix-filler interfaces. This, in turn can augment the load-bearing capacity of the composite films by facilitating a more effective stress transfer mechanism between the nanofillers and the matrix typically leads to enhanced tensile strength, modulus, and toughness.[47] However, a decline in toughness (area under stress *vs.* strain) and elongation of the material is observed, possibly due to reduced polymer chain mobility resulting from improved matrix-filler adhesion. Interestingly, this reduction in toughness does not compromise the flexibility of the matrix.

Beyond the optimal concentration, excess filler tends to form agglomerates due to increased particle-particle interactions. These agglomerates act as stress-concentration sites and defects, reducing the load-bearing efficiency of the composite and causing a decline in mechanical strength and elongation. Notably, the tensile strength of the samples decreases for blends loaded with 10 phr of nHA; attributed to filler agglomeration exceeding a threshold limit.

3.6. Thermogravimetric analysis

Fig. 8a and b represent the result of the thermogravimetric analysis of the samples. All the samples showed the pattern of a two-step degradation. The first stage (320 to 340 °C) corresponds to the breakdown of low-molecular-weight segments and urethane linkages, while the second major degradation stage (around 370 to 410 °C) is associated with decomposition of the hard segments and the cellulose acetate backbone. For composite material, the trend has been shifted to a higher temperature, as can be seen from the plateau portion of the thermograms. Upon incorporation of nHA, it has been observed that both the onset degradation temperature and T_{50} (temperature corresponding to 50% mass loss) shift to higher values, demonstrating a clear improvement in thermal stability. This enhancement arises from multiple synergistic effects comprising the ability of thermally robust ceramic nHA particles to act as heat-diffusion barriers, which reduces the rate of thermal propagation, strong polymer-filler interfacial interactions that restrict molecular mobility, and delayed chain scission. Further, uniformly dispersed can nHA promotes

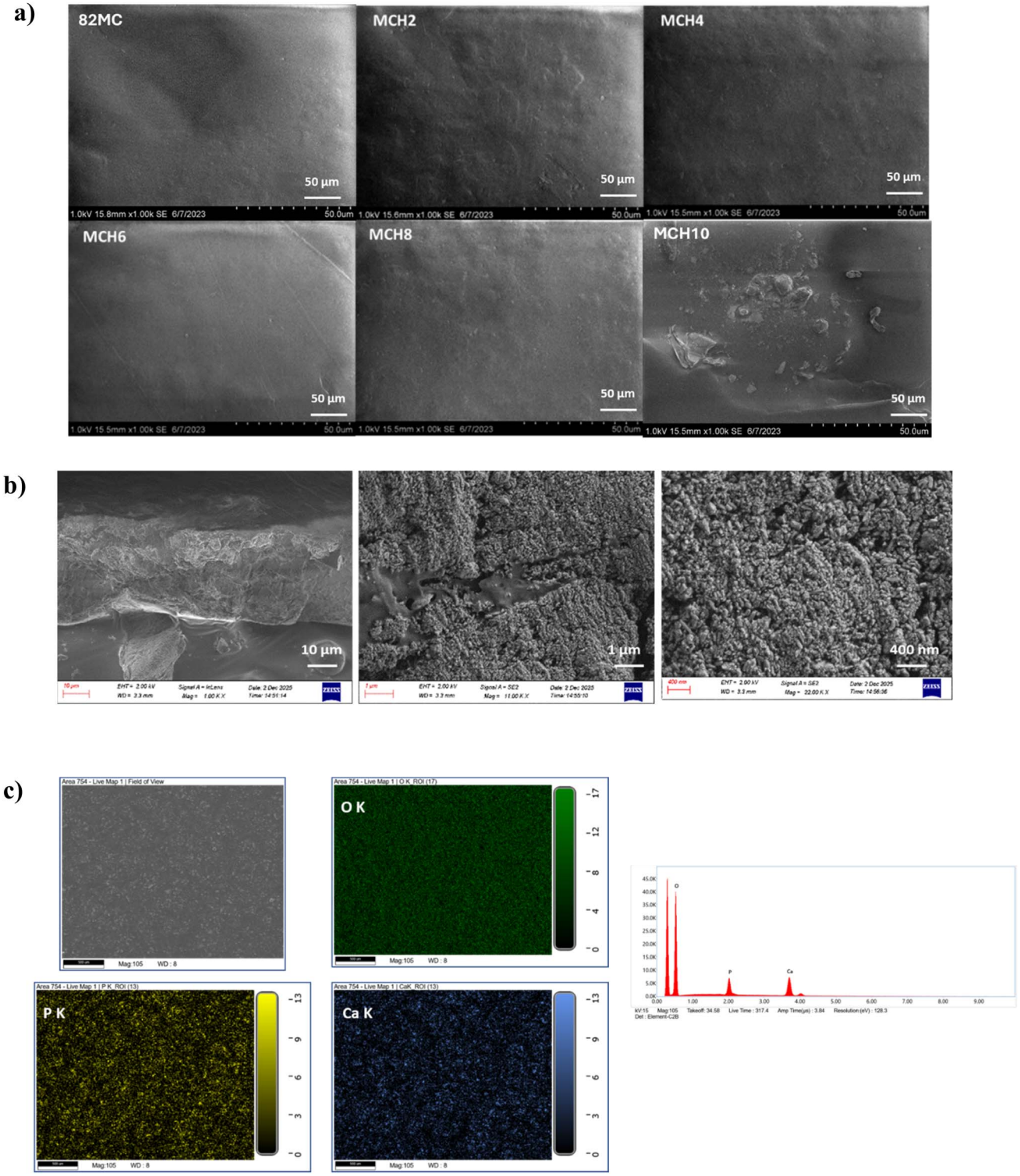

Fig. 6 (a) SEM micrographs of blend and nHA-loaded composite films (b) Cross-sectional SEM micrographs of MCH8 (c) EDAX mapping of MCH8.

higher char formation, as reflected in the increased residue at 600 °C. All the composite films were found to be stable above 300 °C, showing their efficiency for high-temperature applications.

3.7. Dielectric features

Fig. 9a and b depict the variation of the dielectric constant and dielectric loss, respectively, as a function of frequency for different filler loadings within MPU/CA blends. The selected

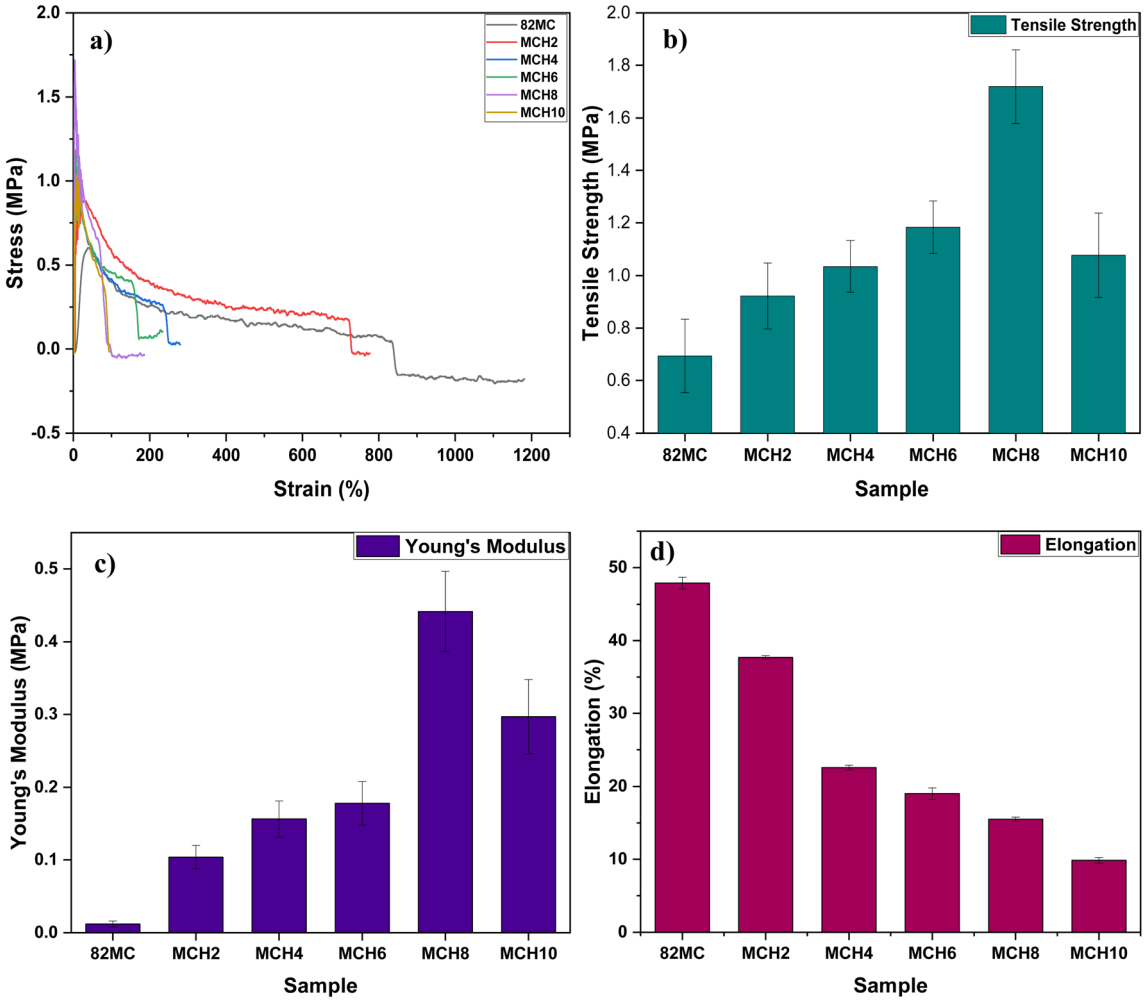

Fig. 7 Mechanical properties of MPU/CA/nHA composite films (a) stress–strain (b) tensile strength (c) Youngs Modulus (d) elongation.

frequency range spans from 40 Hz to 1 MHz. Conspicuously, at lower frequencies, both the dielectric constant and loss exhibit higher values, gradually decreasing as the frequency increases. The frequency-dependent behaviour of the dielectric properties in the developed composite materials can be rationalized by the presence of two types of polarization within the system. Interfacial polarization arises, wherein dipoles form at the interface between the filler and matrix due to their heterogeneity,

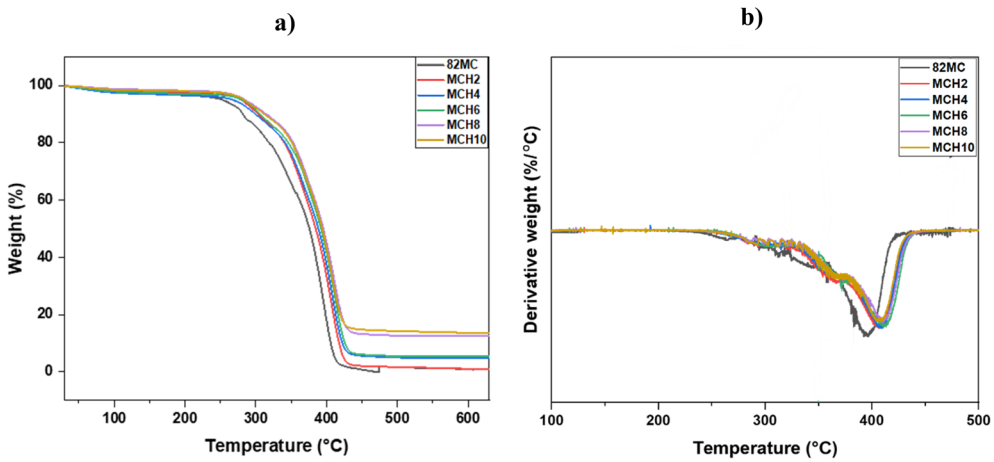

Fig. 8 Thermal stability of MPU/CA/nHA composite samples (a) TGA (b) differential TGA.

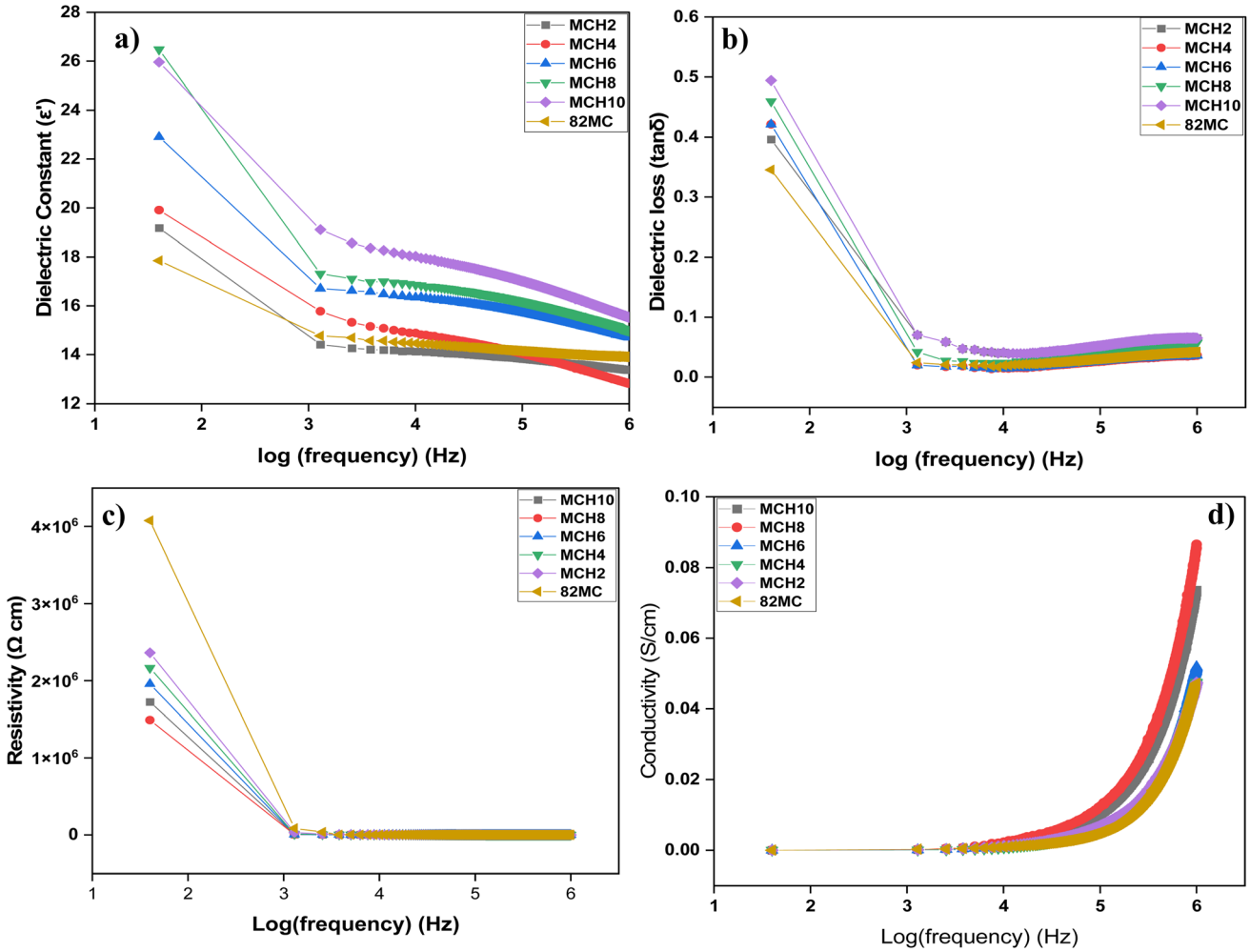

Fig. 9 Dielectric features of MPU/CA/nHA composites (a) dielectric constant (b) dielectric loss (c) resistivity (d) conductivity.

a phenomenon known as Maxwell–Wagner polarization.[48] Additionally, orientational polarization is possible due to the inherent polar nature of both nanohydroxyapatite (nHA) and the matrix components (MPU/CA).[29] At lower frequencies, interfacial polarization between the polymer matrix and filler particles may dominate, with dipoles orienting in the direction of the applied electric field, thereby enhancing the dielectric constant. However, at higher frequencies, interfacial polarization becomes less effective due to limited time for charge accumulation.[49] The dielectric properties of MPU/CA and nanocomposites may also be influenced by dispersion and relaxation phenomena. Molecular or segmental relaxations within the polymer matrix occur more rapidly at higher frequencies, limiting their contribution to the dielectric constant.

Fig. 9c and d depict the electrical resistivity and conductivity of nanohydroxyapatite (nHA)-filled composites, respectively. The resistivity is observed to be higher at low frequencies which decreases as the frequency increases and eventually reaching a frequency-independent state at higher values. This behavior can be viewed in terms of the changes in the polarization process, wherein dipoles lack sufficient time to orient themselves at higher frequencies. Consequently, the dipoles generated by filler particles become ineffective beyond a limiting frequency.[50,51] Conversely, a corresponding

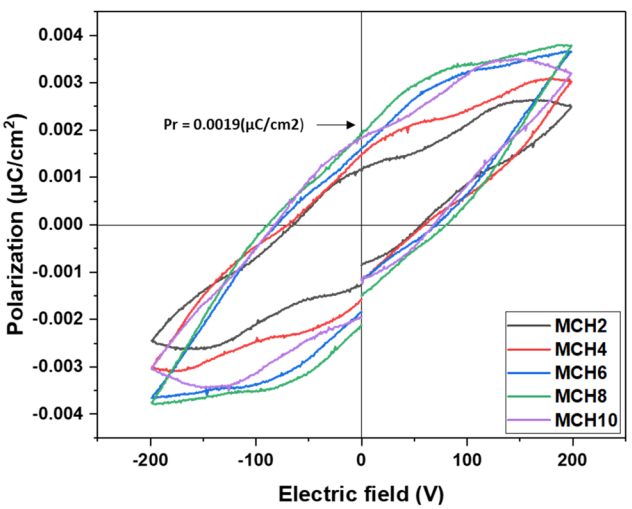

Fig. 10 P–E hysteresis curves of composite films.

enhancement in conductivity is observed, complementing the resistivity trend. This improvement is attributed to the superior piezoelectric response of the composites.

3.8. Ferroelectric features of composite films

To assess the ferroelectric characteristics of the specimens, an electric field ranging from −200 to 200 V was applied, and the ensuing polarization response was scrutinized. The polarization *vs.* electric field (P–E) curves corresponding to the samples are presented in Fig. 10. All composite samples displayed well-defined hysteresis loops and polarization reversal, a distinctive trait of ferroelectric materials.[52] A deviation from ideal ferroelectric curves was observed can be attributed to possible imperfections or defects within the composites. Samples EH8 and EH10 exhibited a maximum remnant polarization (Pr) of 0.0019 μC cm^{-2}, along with a saturation polarization (Ps) of 0.0044 μC cm^{-2}. The presence of ferroelectric domains in the composite materials was thus confirmed, and the viability of these domains for the development of ferroelectric storage devices was indicated by a non-zero value of Pr.

3.9. DC-EFM analysis

To affirm the ferroelectric and piezoelectric characteristics of the specimens, DC-EFM analysis was performed on the MCH4 and MCH8 samples. An applied voltage ranging from −10 V to +10 V facilitated the examination of phase and amplitude variations in the samples. Fig. 11a–d depict the amplitude and EFM phase curves corresponding to the respective voltages.

The inclusion of nano-hydroxyapatite (nHA) as a filler within the dielectric MPU/CA matrix gives rise to a significant number of internal dipoles. The piezoelectric effect induces the alignment of these internal dipoles, resulting in a measurable strain represented in terms of voltage.[53] The amplitude curves correspond to the piezoelectric strain present in the material, and an

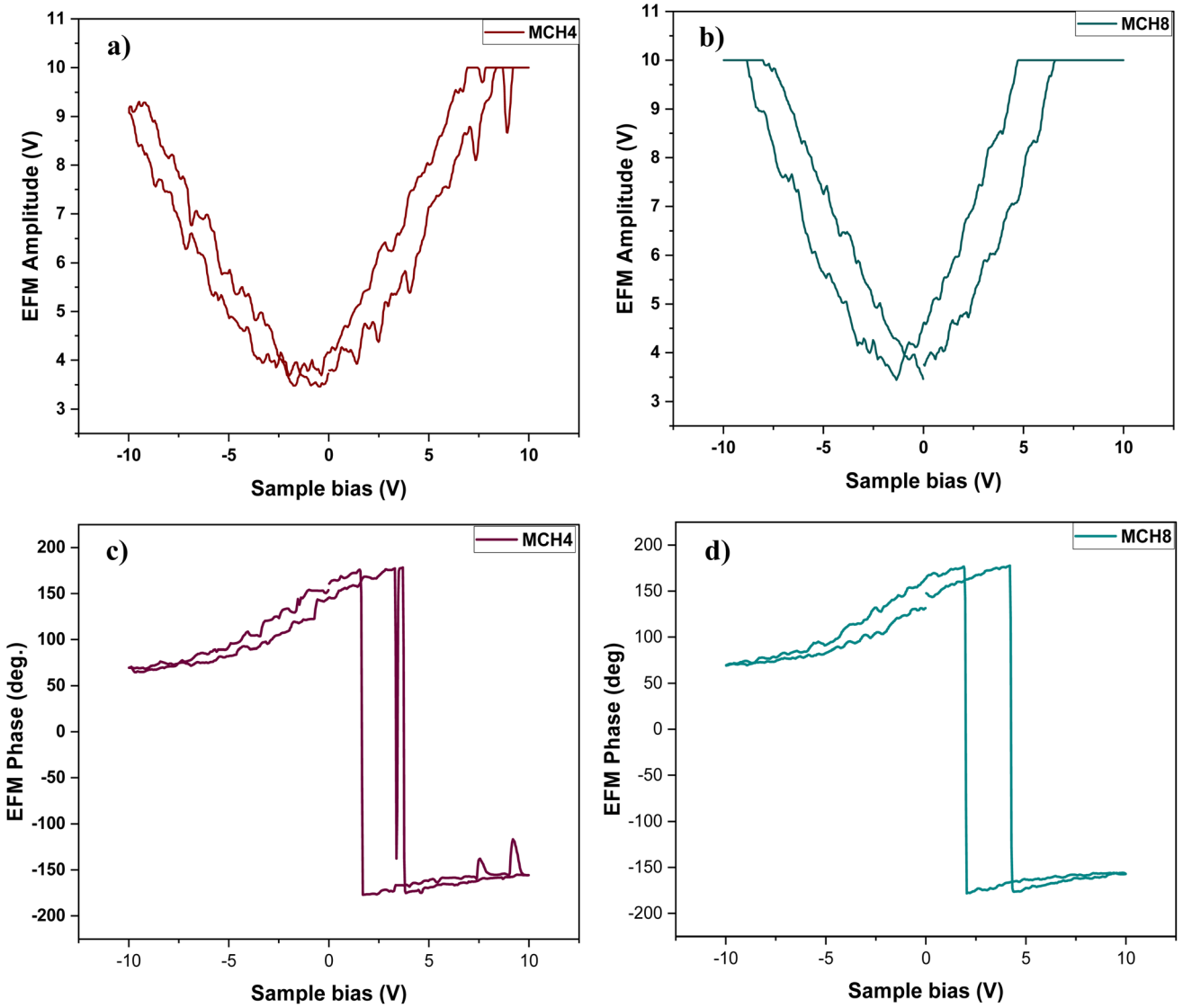

Fig. 11 (a) DC-EFM amplitude curve for 4phr nHA loaded composite films (b) DC-EFM amplitude curve for 8phr nHA loaded composite films (c) DC-EFM phase curves for 4phr nHA loaded composite films (d) DC-EFM phase curves for 8phr nHA loaded composite films.

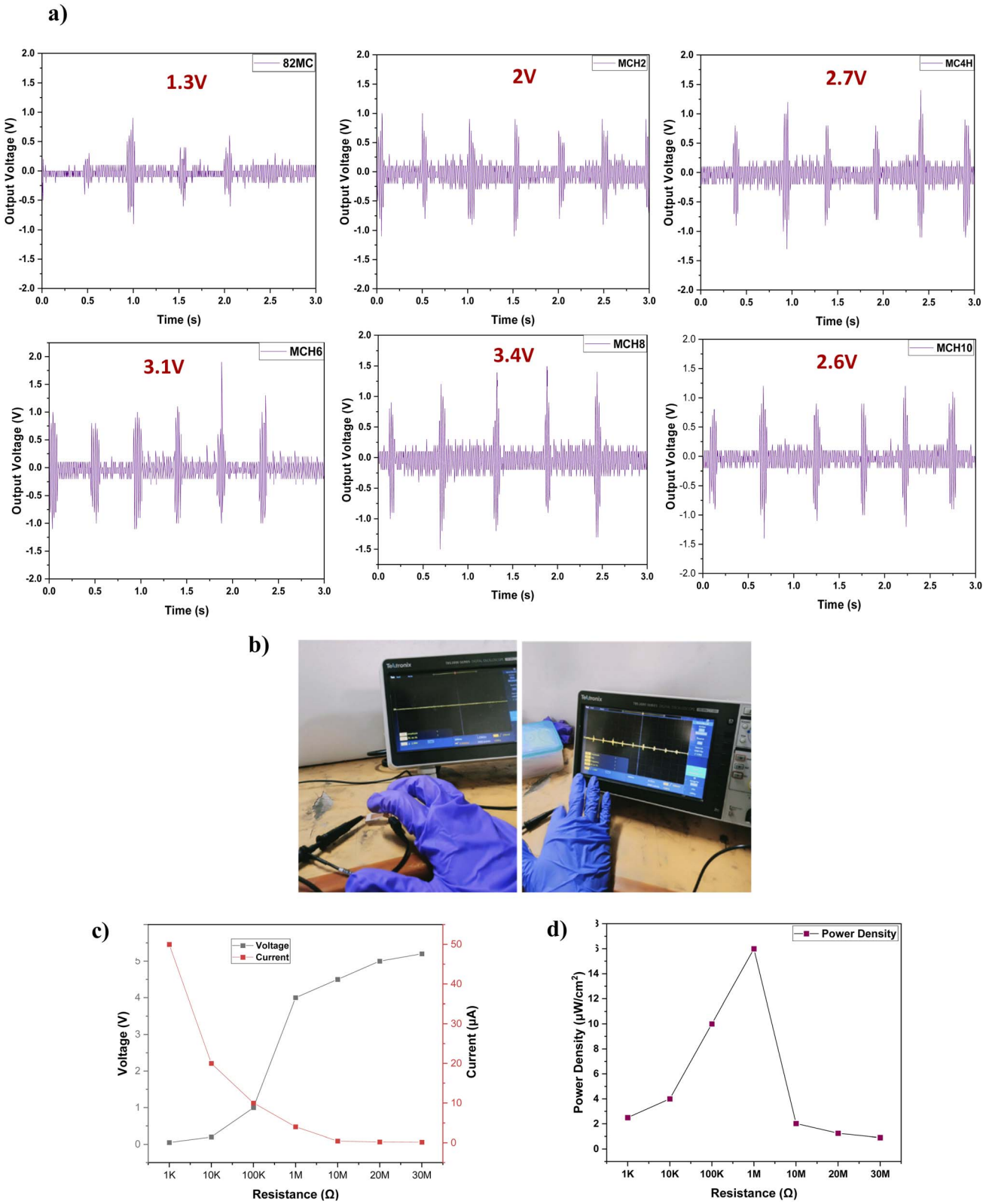

Fig. 12 (a) Output voltage generated for each sample corresponding to finger-tapping (b) photograph showing output voltage generation in response to finger-tapping (c) voltage–current output data as a function of external load resistance (d) power density for variable load resistance.

augmentation in strain amplifies the associated EFM amplitude. EFM phase curves illustrate the capacity of the dipoles to undergo spontaneous polarization and exhibit polarization reversal properties under the influence of applied voltage. This switching of orientation signifies the ferroelectric nature of the composite materials.[54] The observation of butterfly-shaped

amplitude curves and well-defined hysteresis in the EFM phase for the samples unequivocally indicates the presence of ferro-piezoelectric characteristics in the material.

3.10. Output voltage generation performance

For the examination of commercial viability, a device prototype was fabricated by encapsulating the composite film (1 cm × 1 cm) between two copper plates to evaluate its performance in voltage generation. The assembled device was linked to a digital oscilloscope, and the voltage produced under compressive forces from human fingers was recorded. Fig. 12a illustrates the voltage output from each sample during the finger-tapping process. The pristine polymer blend exhibited a voltage of 1.3 V, likely arising from friction between the dielectric matrix components (MPU/CA), associated with triboelectricity.[55] The MCH8 system with 8 phr nHA achieved a maximum voltage of 3.4 V, while other samples yielded voltages of 2.1, 2.7, 3.1, and 2.6 V for MCH2, MCH4, MCH6, and MCH10, respectively. The voltage output signal displayed well-defined alternate positive and negative peaks, attributed to an interfacial polarization between the filler and matrix. The application of pressure disturbs the dipole orientation, generating a positive signal, and upon the release of force, the dipole reorients, generating a negative peak.[56] Considering the dielectric constant values and observed polarisations, the cumulative output from the samples can be attributed to a combination of piezoelectric and triboelectric features, ie, tribo-piezoelectricity. The triboelectric output may be attributed to the heterogeneous interfaces within the composite (MPU/CA, polymer/nHAp, and composite/electrode), which could induce Maxwell–Wagner–Sillars interfacial polarization under mechanical stress, enhancing charge trapping and voltage generation. This effect is further supported by the micro-roughness introduced by nHAp particles and the inherent tribonegative sites of cellulose acetate.

Increasing filler loading naturally increases the bulk dielectric constant of the composite because of the intrinsically high permittivity of nHA. However, at high loading, nHA particles tend to agglomerate, forming clusters of bulk filler content. Agglomerated filler clusters trap charges instead of transferring them. Although the dielectric permittivity increases with filler loading, the highest output voltage is observed for MCH8, as it provides the most effective interfacial polarization. SEM analysis (Fig. 6a) shows that MCH8 exhibits a well-dispersed nHA network with strong polymer–filler interfacial contact, which maximizes Maxwell–Wagner–Sillars (MWS) interfacial polarization and facilitates efficient stress-induced charge separation. In contrast, the MCH10 system contains visible nHA agglomerates that, while contributing to a higher bulk dielectric constant (Fig. 9a), reduce the effective interfacial area and disrupt charge-transfer pathways, which eventually affects the overall output voltage.

The short circuit current–voltage (I–V) characteristics and power density (Pd) of the prototype were evaluated for the optimized sample MCH8, across load resistances ranging from 1 kΩ to 30 MΩ, as presented in Fig. 12c and d, respectively. The corresponding current and power density were subsequently determined using (eqn (2)) and (eqn (3)).[57]

$$I = \frac{V}{\mathrm{RL}} \tag{2}$$

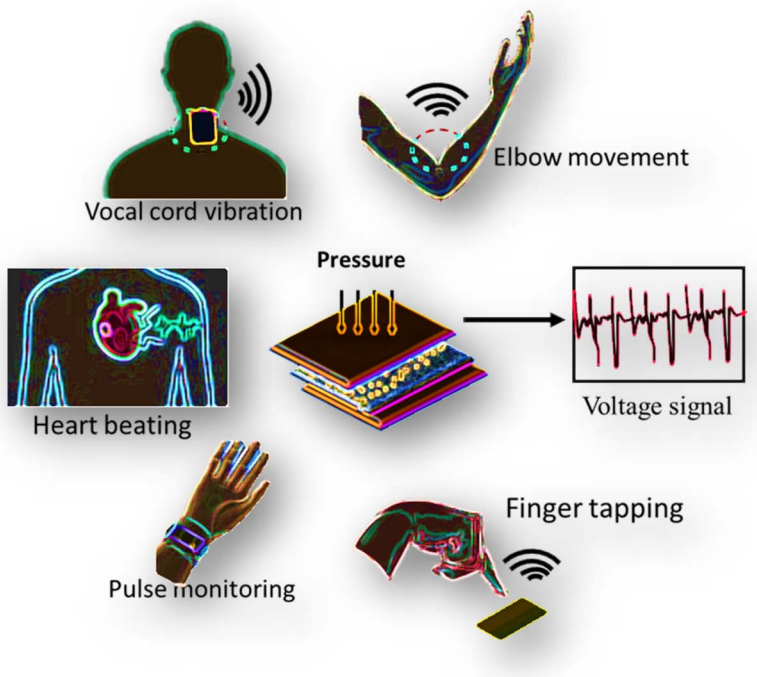

Fig. 13 Piezoelectric nanogenerator for human physiological motion sensing applications.

$$\mathrm{Pd} = \frac{V^2}{\mathrm{RL} \times A} \quad (3)$$

where I is the short circuit current, V is the output voltage (V), RL is the load resistance (Ω), Pd is the power density (μW cm^{-2}), and A is the active area (cm^2).

The prototype exhibited its highest performance at a load resistance of 1 MΩ, where it delivered a maximum power density (P_{max}) of 16 μW cm^{-2} along with the highest short-circuit current of 50 μA. This optimal output at intermediate resistance reflects the balance between voltage buildup at higher loads and current flow at lower loads, confirming 1 MΩ as the most efficient operating condition for the device.

Our preliminary experiments with the fabricated device demonstrate the feasibility of affixing flexible composites to a patient's body to enhance their signaling capabilities as needed, particularly for capturing the attention of bystanders when a patient is bedridden, especially at night. A biosensor design, inspired by the concept depicted in Fig. 13, is presently are being tested for real-time applications in our laboratory.

4. Conclusion

Flexible tribo-piezoelectric systems have been developed based on MPU, CA and nHA. The MPU/CA/nHA films have initially been characterized through FTIR, XRD, TGA, and UTM to ensure the required physico-chemical characteristics for the nanogenerators. The addition of fillers has been found to improve the mechanical properties of the composite films. For practical utilization, the piezoelectric nature of the composite films was confirmed by evaluating butterfly-shaped amplitude curves obtained from DC-EFM. The examination of ferroelectric features was accomplished through P-E hysteresis curves. A device prototype was constructed, and tribo-piezoelectric responses were examined through random finger tapping, utilizing a digital oscilloscope. An optimized system with an 8phr nHA loading yielded a voltage of 3.4 V. These results suggest a promising avenue for the development of a user-friendly, flexible nanogenerator for commercial applications.

Author contributions

Gopika Melepalliyalil: designing the work, methodology, investigation, writing – original draft. Mekha Mariam Mathew: data analysis, writing, editing. Soney Varghese: validation, resources. Unnikrishnan Gopalakrishna panicker: supervision, editing and review.

Conflicts of interest

The authors hereby declare that there is no conflict of interest or have no known competing financial interests and satisfy all ethics in publishing policy.

Data availability

Data will be made available upon reasonable request.

Acknowledgements

The authors gratefully acknowledge CIF for instrumentation facilities, University of Calicut for FE-SEM facility, C-MET, Thrissur, for impedance analyzer, and Sree Kerala Varma College for the ferroelectric tester. G. M. is thankful to NIT Calicut for her fellowship.

References

1 P. Costa, J. Nunes-Pereira, N. Pereira, N. Castro, S. Gonçalves and S. Lanceros-Mendez, *Energy Technol.*, 2019, **7**, 1800852.
2 Q. Lin, R. Xue, Y. Huang, Y. Wu and Q. Shi, *Polym. Bull.*, 2024, **20**, 1–8.
3 S. Priya, H. C. Song, Y. Zhou, R. Varghese, A. Chopra, S. G. Kim, I. Kanno, L. Wu, D. S. Ha, J. Ryu and R. G. Polcawich, *Energy Harvest. Syst.*, 2017, **4**, 3–39.
4 G. S. Ekbote, M. Khalifa, B. V. Perumal and S. Anandhan, *RSC Appl. Polym.*, 2023, **1**, 266–280.
5 F. Narita and M. Fox, *Adv. Eng. Mater.*, 2018, **20**, 1700743.
6 N. P. Raj, N. R. Alluri, G. Khandelwal and S. J. Kim, *Compos. Part B Eng.*, 2019, **161**, 608–616.
7 X. Niu, W. Jia, S. Qian, J. Zhu, J. Zhang, X. Hou, J. Mu, W. Geng, J. Cho, J. He and X. Chou, *ACS Sustainable Chem. Eng.*, 2018, **7**, 979–985.
8 M. B. Khan, D. H. Kim, J. H. Han, *et al.*, *Nano Energy*, 2019, **58**, 211–219.
9 H. Wei, H. Wang, Y. Xia, D. Cui, Y. Shi, M. Dong, C. Liu, *et al.*, *J. Mater. Chem. C*, 2018, **6**, 12446–12467.
10 R. Theissmann, L. A. Schmitt, J. Kling, R. Schierholz, K. A. Schönau, H. Fuess, M. Knapp, H. Kungl and M. J. Hoffmann, *J. Appl. Phys.*, 2007, **102**, 024111.
11 M. Smith and S. Kar-Narayan, *Int. Mater. Rev.*, 2022, **67**, 65–88.
12 K. S. Ramadan, D. Sameoto and S. Evoy, *Smart Mater. Struct.*, 2014, **23**, 033001.
13 S. Deswal, S. Arab, N. He, W. Gao, B. Lee and V. Misra, *RSC Appl. Polym.*, 2024, **2**, 634–641.
14 D. Singh, A. Choudhary and A. Garg, *ACS Appl. Mater. Interfaces*, 2018, **10**, 2793–2800.
15 A. Barjola Ruiz, O. Sahuquillo Navarro, A. Sonseca Olalla, V. Compañ Moreno and E. Giménez Torres, *J. Mater. Chem. C*, 2025, **13**, 15451–15460.
16 J. Zhang, D. Liu, Q. Han, *et al.*, *Compos. Part B Eng.*, 2019, **175**, 107157.
17 S. Siddiqui, D.-I. Kim, E. Roh, *et al.*, *Nano Energy*, 2016, **30**, 434–442.
18 B. H. Moghadam, M. Hasanzadeh and A. Simchi, *ACS Appl. Nano Mater.*, 2020, **3**, 8742–8752.
19 A. Mondal, H. H. Singh and N. Khare, *J. Mater. Sci.:Mater. Electron.*, 2023, **34**, 314.
20 S. Y. Chung, S. Kim, J.-H. Lee, *et al.*, *Adv. Mater.*, 2012, **24**, 6022–6027.
21 Z. Pi, J. Zhang, C. Wen, *et al.*, *Nano Energy*, 2014, **7**, 33–41.
22 O. Sanches, M. J. da Silva, L. F. Malmonge, N. R. Basso and J. A. Malmonge, *J. Appl. Polym. Sci.*, 2021, **138**, 50865.

23 F. C. M. Freire Filho, J. A. Santos, A. O. Sanches, *et al.*, *J. Appl. Polym. Sci.*, 2023, **140**, e53572.
24 J. Yan, M. Lv, Y. Qin, *et al.*, *ACS Appl. Nano Mater.*, 2023, **6**, 5675–5684.
25 Y. Li, Q. Hu, R. Zhang, W. Ma, S. Pan, Y. Zhao, Q. Wang and P. Fang, *Mater.*, 2022, **15**, 7026.
26 V. Saxena, L. Pandey and T. S. Srivatsan, *Curr. Nanomater.*, 2021, **6**, 207–221.
27 T. T. Luu, N. D. Huynh, H. Kim, Z.-H. Lin and D. Choi, *Nanoscale*, 2023, **15**, 14205–14214.
28 P. Sathiyanathan, D. M. Dhevi, A. A. Prabu and K. J. Kim, *Macromol. Res.*, 2019, **27**, 743–749.
29 V. H. Shafeeq, S. C. Karumuthil, J. K., S. Varghese, S. Athiyanathil and U. G. Panicker, *ACS Appl. Mater. Interfaces*, 2021, **13**, 24106–24116.
30 H. Joo, S. Gwak, M. H. Lee, H. Park, C. Lee, J. H. Lee, S. A. Han and J.-H. Lee, *Sustain. Mater. Technol.*, 2023, **36**, e00638.
31 V. A. Cao, M. Kim, P. C. Van, J.-R. Jeong, S. Y. Kim and J. Nah, *J. Mater. Chem. A*, 2024, **12**, 3142–3150.
32 Y. Yang, Z.-S. Gao, M. Yang, *et al.*, *Nano Energy*, 2019, **59**, 363–371.
33 V. H. Shafeeq and G. Unnikrishnan, *J. Polym. Res.*, 2020, **27**, 53.
34 J. H. Mo, J. Y. Kim, Y. H. Kang, S. Y. Cho and K. S. Jang, *ACS Sustainable Chem. Eng.*, 2018, **6**, 15970–15975.
35 A. Gandhi, M. Wojtas, S. B. Lang, A. L. Kholkin and S. A. Tofail, *J. Am. Ceram. Soc.*, 2014, **97**, 2867–2872.
36 M. Bindu and G. Unnikrishnan, *Phys. Chem. Chem. Phys.*, 2017, **19**, 25380–25390.
37 K. Juraij, V. H. Shafeeq, A. M. Chandran, *et al.*, *J. Mater. Sci.*, 2023, **58**, 317–336.
38 M. Kang, D.-M. Lee, I. Hyun, N. Rubab, S.-H. Kim and S.-W. Kim, *Chem. Rev.*, 2023, **123**, 11559–11618.
39 D. Choi, Y. Lee, Z.-H. Lin, S. Cho, M. Kim, C. K. Ao, S. Soh, *et al.*, *ACS Nano*, 2023, **17**, 11087–11219.
40 A. Tozar and I. H. Karahan, *Bioinspired Biomim. Nanobiomater.*, 2018, **7**, 149–158.
41 S. S. Chandrasekar and A. Dakshnamoorthy, *Int. J. Phys. Sci.*, 2013, **8**, 1639–1645.
42 J. Jayadevan, R. Alex and U. Gopalakrishnapanicker, *Int. J. Biol. Macromol.*, 2018, **107**, 1821–1834.
43 R. Rarima and G. Unnikrishnan, *Polym. Degrad. Stab.*, 2020, **177**, 109187.
44 J. Reyes-Gasga, E. L. Martínez-Piñeiro, G. Rodríguez-Álvarez, *et al.*, *Mater. Sci. Eng., C*, 2013, **33**, 4568–4574.
45 M. C. Barbosa, N. R. Messmer, T. R. Brazil, *et al.*, *Mater. Sci. Eng., C*, 2013, **33**, 2620–2625.
46 A. Ślósarczyk, Z. Paszkiewicz and C. Paluszkiewicz, *J. Mol. Struct.*, 2005, **744**, 657–661.
47 L. Alexander and H. P. Klug, *J. Appl. Phys.*, 1950, **21**, 137–142.
48 H. Lu, X. Zhang and H. Zhang, *J. Appl. Phys.*, 2006, **100**, 054104.
49 M. Samet, V. Levchenko, G. Boiteux, *et al.*, *J. Chem. Phys.*, 2015, **142**, 194703.
50 C. Ellingford, C. Wan, Ł. Figiel and T. McNally, *Compos. Commun.*, 2018, **8**, 58–64.
51 R. Jose, L. A. Varghese and U. G. Panicker, *Polym. Bull.*, 2022, **79**, 2041–2060.
52 K. Chen and Y. Jiao, *Front. Mater. Sci.*, 2017, **11**, 59–65.
53 V. H. Shafeeq, C. K. Subash, S. Varghese and G. P. Unnikrishnan, *Polym. Int.*, 2020, **69**, 1256–1266.
54 C. He, Z. Wang, X. Li, X. Yang, X. Long and Z. G. Ye, *Acta Mater.*, 2017, **125**, 498–505.
55 W.-S. Jung, M.-G. Kang, H.-G. Moon, *et al.*, *Sci. Rep.*, 2015, **5**, 9309.
56 S. K. Ghosh, P. Adhikary, S. Jana, *et al.*, *Nano Energy*, 2017, **36**, 166–175.
57 M. M. Mathew, N. Jones and U. G. Panicker, *Chem. Eng. J.*, 2025, 170090.